

—Supporting Information—

## Capillary forces between sediment particles and an air-water interface

Nirmalya Chatterjee<sup>1,\*</sup>, Sergey Lapin<sup>2</sup> and Markus Flury<sup>1</sup>

<sup>1</sup>*Department of Crop and Soil Sciences, Washington State University, Puyallup, WA 98371, USA.* <sup>2</sup>*Department of Mathematics, Washington State University, Pullman, WA 99164.*

*\*Corresponding author, Phone: +1-509-432-9533, c\_nirmalya@wsu.edu*

Supporting information contains details on the theoretical calculations, measurement precision, calculation of volume-equivalent dimensions. Also given are tables with particle characterization data, experimental force measurements, and particle volume measurements. Figures show dissection scope images of particles, experimental schematics, and force-position plots.

## S.1 Derivation of Force Balance on an Ellipsoidal Particle at the Air-Water Interface

First, we define the symbols that we use below:

$a, b, c$	semi-principal axes of an ellipsoidal particle in the $x, y, z$ coordinate axes		
$e_{xy}$	eccentricity of the ellipses of cross-section on the $xy$ plane containing the contact line		
$e_{xz}$	eccentricity of the ellipse of cross-section on the $xz$ plane normal to both the plane of the contact line and the $y$ -axis		
$f$	total force	$f_b$	buoyancy force
$f_{DLVO}$	DLVO force	$f_p$	hydrostatic pressure force
$f_s$	surface tension force	$f_w$	gravity force
$g$	acceleration due to gravity	$r$	radius of the spherical particle
$x_c$	distance of the three-phase contact line on the $x$ -axis from the vertical ( $z$ -axis)		
$z_c$	deflection depth, i.e., the depth of the well formed in the air-water interface due to the presence of the particle		
$\beta$	the angle of inclination of the projection of the air-water interface at the three-phase contact line on (for an ellipsoidal particle on the surrounding sphere with radius = largest of the semi-major axes, also called the parametric latitude)		
$\Delta p_c$	pressure difference across the air-water interface		
$\phi_c$	the angle of inclination of the air-water interface at the three-phase contact line of a sphere		
$\kappa$	ratio of length of contact line for an ellipsoidal particle (undulating / flat)		
$\gamma$	surface tension of water	$\theta$	contact angle
$\rho_l$	density of liquid phase (water)	$\rho_g$	density of gas phase (air)
$\Delta\rho$	$(\rho_l - \rho_g)$	$\rho_s$	density of solid phase (particle)

We derive the force balance equation for an ellipsoid by generalizing the theory for a sphere. The theory for a sphere has been described previously (1–3). Here, we use a similar notation as in Zhang et al. (2).

**Sphere:** For a sphere, the gravity and buoyancy forces are given as:

$$f_w = \frac{4}{3}\pi r^3 \rho_s g \quad (\text{S.1})$$

$$f_b = -\frac{\pi}{3}r^3 \rho_l g [2 + 3 \cos(\phi_c + \theta)) - \cos^3(\phi_c + \theta)] \quad (\text{S.2})$$

The surface tension force is given as (2,3):

$$f_s = 2\pi x_c \gamma \sin \phi_c = 2\pi r \gamma \sin(\phi_c + \theta) \sin \phi_c \quad (\text{S.3})$$

The hydrostatic pressure force is (2,3):

$$f_p = \pi x_c^2 \Delta p_c = \pi r^2 \rho_l g z_c \sin^2(\phi_c + \theta) \quad (\text{S.4})$$

Quantitative measurements of the forces exerted by the air-water interface often involve the use of a process tensiometer where the particle is suspended from a microbalance and then dipped into a liquid (Figure S.4). In such an experimental setup, the microbalance with the particle suspended is tared in the air-phase, so that  $f_{\text{DLVO}} = 0$  and  $f_w = 0$ , and the force balance for a sphere (Eq. 1) becomes (1-3):

$$f = 2\pi r \gamma \sin(\phi_c + \theta) \sin \phi_c + \pi r^2 \Delta \rho g z_c \sin^2(\phi_c + \theta) - \frac{\pi}{3} r^3 \Delta \rho g [2 + 3 \cos(\phi_c + \theta) - \cos^3(\phi_c + \theta)] \quad (\text{S.5})$$

**Ellipsoid:** For an ellipsoid (Figure S.1), the gravity force is given as:

$$f_w = \frac{4}{3}\pi abc \rho_s g \quad (\text{S.6})$$

The buoyancy force for a partially immersed ellipsoid is:

$$f_b = -\frac{\pi}{3} abc \rho_l g \left[ 2 - 3 \cos(\beta + \frac{\pi}{2}) + \cos^3(\beta + \frac{\pi}{2}) \right] \quad (\text{S.7})$$

The angle  $\beta$ , also called the parametric latitude, is calculated from the angles  $\theta$  and  $\phi_c$  as:

$$\beta = \arctan \left[ (\sqrt{1 - e_{xz}^2}) \tan \left( \frac{3\pi}{2} - \theta - \phi_c \right) \right] = \arctan \left[ \frac{c}{a} \tan \left( \frac{3\pi}{2} - \theta - \phi_c \right) \right] \quad (\text{S.8})$$

where the eccentricities of the ellipses  $e_{xy}$  and  $e_{xz}$  are defined as:

$$e_{xy} = \sqrt{1 - \frac{b^2}{a^2}} \quad (\text{S.9})$$

$$e_{xz} = \sqrt{1 - \frac{c^2}{a^2}} \quad (\text{S.10})$$

The surface tension force, which depends on the length of the three-phase contact line, is given as:

$$f_s = 4a\kappa E(e_{xy})\gamma \sin \phi_c \sin \beta \quad (\text{S.11})$$

where  $E(e_{xy})$  is the complete elliptic integral of the second kind for an ellipse on the  $xy$  plane (plane of the three-phase contact line) and  $\kappa$  is the ratio of the lengths of the undulating contact line to the flat elliptic contact line (see next sub-section). The surface tension force can be either upward (if  $\phi_c + \theta > 180^\circ$ ) or downward (if  $\phi_c + \theta < 180^\circ$ ).

The hydrostatic pressure force is:

$$f_p = \pi ab \Delta p_c = \pi ab \rho_l g z_c \sin^2(\beta) \quad (\text{S.12})$$

For a tared ellipsoidal particle in the air-phase, the final force balance equation (Eq. 1) then becomes:

$$f = 4a\kappa E(e_{xy})\gamma \cos \beta \sin \phi_c + \pi ab \Delta \rho g z_c \cos^2 \beta - \frac{\pi}{3} \Delta \rho g abc (2 + 3 \sin \beta - \sin^3 \beta) \quad (\text{S.13})$$

### **Calculating the undulating quadrupolar contact line on an ellipsoidal particle.**

Previous work has shown that the contact line at the liquid-gas interface on an asymmetric particle, like an ellipsoid, is not planar, but in fact undulates, and can be described using a quadrupolar expansion (4–10). We used the approach of van Nierop et al. (8) to calculate the undulation of the interface line for an ellipsoid. We assume that the mean position of the contact line is the same as the one at a flat contact line, as would be present on a symmetrical (i.e., circular cross-section) particle.

The undulation is described as a deviation of the contact line from its mean position on the  $z$ -axis. The deviation  $z_{dev}$  on the the  $z$ -axis is calculated as a solution of the equation (8):

$$\sum_{n=1}^{\infty} \frac{C_n \cos(2n\varphi)(1 - e_{xy}^2 \cos^2 \varphi)^n}{\{1 - (z_{dev} - C_0)^2\}^n} - z_{dev} = 0 \quad (\text{S.14})$$

where  $-\pi \leq \varphi \leq \pi$  is the azimuthal angle of the point  $z_{dev}$ ,  $C_0$  and  $C_n$  are coefficients, and  $e_{xy}$  is the eccentricity of the ellipse cross-section at the contact line (see Eq. S.9).

The series was summed until  $n = 2$  as the contribution of higher-order terms quickly falls off. The resulting undulations  $z_{dev}$  were two orders of magnitude smaller ( $< 1\%$ ) than the respective  $c$  values (semi-major axis on the  $z$ -axis) of the particle. An optimization of the coefficients  $C_n$ , which enforces the contact angle between the air-water interface and the ellipsoidal surface was thus not attempted. The initial set of  $C_n$  used was  $[C_0, C_1, C_2] = -\cos(\theta)[1, 0.01, 0.0001]$  (8).

The length of the undulating contact line was calculated by summing the distance between the previously calculated points using Eq. S.14. A similar calculation was done assuming a flat, elliptic contact line. The increase in contact line due to the undulation was expressed as  $\kappa$ , the length ratio of the undulating line to the flat line (Table S.3). The effect of the undulating contact line length is an increase of the capillary force (Table S.3).

## S.2 Calculation of a Volume-Equivalent Radius and Semi-Major Axes for a Particle

For each particle we calculated a volume-equivalent radius, corresponding to the radius of a sphere with the same volume as the particle, as well as the semi-major axes corresponding to a volume-equivalent ellipsoid. To determine the particle volume, we measured the buoyancy force from the force-position curves of the dry particle at the point just after the snap-off of

the air-water interface. The measured buoyancy force was then corrected for the buoyancy of the submerged portion of the steel J-hook attached to the particle (Figure S.4) as well as for the surface tension force on the submerged part of the hook. The corrected buoyancy force,  $f_{buoy,corr}$  is given as:

$$f_{b, \text{ corr}} = f_{b, \text{ uncorr}} - f_{b, \text{ hook}} + f_{s, \text{ hook}} \quad (\text{S.15})$$

The volume of a particle,  $v_p$ , and the volume-equivalent spherical radius,  $r_{ve}$ , are calculated as:

$$v_p = \frac{f_{b, \text{ corr}}}{\rho_l g} \quad (\text{S.16})$$

$$r_{ve} = \sqrt[3]{\frac{3v_p}{4\pi}} \quad (\text{S.17})$$

The volume-equivalent ellipsoidal semi-major axes  $(a, b, c)_{ve}$  were calculated using the spherical  $r_{ve}$  scaled with the rms values of the semi-major axes  $(a, b, c)_{rms}$ , this keeps the volume of the ellipsoid equal to that of the natural particle (and the volume-equivalent sphere). Also, the maximum semi-major axes  $(a, b, c)_{max}$  were used to construct an encompassing ellipsoid of maximum dimensions ( $r_{max}$ ) for comparison to the volume-equivalent ellipsoid. A schematic of the process is shown in Figure S.2. The particle volume and the rms dimension along the  $z$  axis ( $c_{rms}$ ) were used to calculate the radius for the cylinder, which were used in theoretical calculations involving a volume-equivalent cylinder. Results are summarized in Tables S.1 and S.2.

### S.3 Errors of Force-Position Measurements

#### Errors due to change in surface tension of water.

For each particle's sequence of measurements, we used the same water in the glass cup, but we changed the water for every new particle. We measured the surface tension of the

water before and after the determination of each force-position curve with the Wilhelmy plate method. The surface tension of water before immersion of the particle was  $72.4 \pm 0.4$  mN/m, while the surface tension after the uncleaned particle had been immersed was  $65.8 \pm 3.2$  mN/m for basalt, hematite, and mica, and  $72.1 \pm 0.3$  mN/m for the other particles. As the surface tension of the water changed by  $\approx 10\%$  between the start and end of a force-distance sequence, our force measurements are erroneous to maximal 10% when comparing cleaned and uncleaned particle data.

### **Errors due to randomness in roughness of particle surfaces.**

Figure S.5 depicts the precision (measurement error) in the measurement of the capillary forces, illustrated for a smooth particle (PTFE sphere) and a natural sediment particle (quartz). Generally, the errors were larger for the sediment particle than the standard particles because of the slipping and pinning of the interface line caused by surface roughness. The plots show that the standard deviations were largest when the changes of forces with respect to position ( $\Delta f / \Delta z$ ) were greatest, i.e., when snap-off of the interface occurred. This is because the position where snap-off occurs depends on surface roughness, and depending on the degree of surface roughness, snap-off may not occur always at exactly the same location. This effect is more pronounced for the irregularly-shaped quartz particle (Figure S.5b) than for the PTFE sphere (Figure S.5a).

**Table S.1.** Particle characterization in terms of spatial dimensions and contact angle with an air-water interface.

Particle	$r_{ve}^{\S}$	$x_{\max}^{\star}$	$x_{\text{rms}}^{\S\S}$	$y_{\max}^{\star}$	$y_{\text{rms}}^{\S\S}$	$z_{\max}^{\star}$	$z_{\text{rms}}^{\S\S}$	contact angle $^{\dagger}$
	(mm)	(mm)	(mm)	(mm)	(mm)	(mm)	(mm)	( $^{\circ}$ )
PTFE sphere $^{\ddagger}$	3.17	5.59	—	5.56	—	5.57	—	109 $\pm$ 5
PTFE disc $^{\ddagger}$	2.09	4.81 $^d$	—	—	—	2.22 $^t$	—	109 $\pm$ 5
PTFE tent $^{\ddagger}$	2.25	5.99 $^l$	—	4.75 $^b$	—	3.45 $^h$	—	109 $\pm$ 5
Basalt	1.15	3.56	2.64	1.88	1.51	0.96	0.79	67 $\pm$ 3
Granite	1.17	2.92	2.29	2.15	1.62	1.73	1.30	83 $\pm$ 2
Hematite	1.00	2.45	1.99	2.27	1.90	1.47	1.07	95 $\pm$ 1
Magnetite	0.79	2.32	1.72	2.01	1.42	0.95	0.75	84 $\pm$ 2
Mica	0.85	2.71	2.16	1.79	1.44	0.97	0.69	58 $\pm$ 3
Milky Quartz	1.07	2.03	1.58	1.92	1.50	1.69	1.21	117 $\pm$ 2
Quartz	1.13	3.07	2.27	2.44	1.81	1.61	1.28	75 $\pm$ 2

$^{\ddagger}$  single measurements for all PTFE particles hence no rms values are reported

$^{\S}$  volume-equivalent radius

$^{\star}$  maximum dimension

$^{\S\S}$  root mean square dimension

$^{\dagger}$  contact angle for cleaned particles

$^{d,t}$  diameter & thickness of PTFE disc

$^{l,b,h}$  base length, base breadth & height of PTFE tent



**Table S.2.** Particle volume, radius of volume-equivalent sphere ( $r_{ve}$ ) and semi-major axes of volume-equivalent ellipsoids (using both maximum  $a : b : c$  and root-mean-square (rms)  $a : b : c$  ratios).

Particle	volume (mm <sup>3</sup> )	$r_{ve}$ (mm)	rms (mm)			maximum (mm)		
			$a$	$b$	$c$	$a$	$b$	$c$
PTFE sphere	133.90	3.17	3.18	3.17	3.17	3.18	3.17	3.17
PTFE disk	38.17	2.09	2.70	2.70	1.25	2.70	2.70	1.25
PTFE tent	47.51	2.25	2.92	2.31	1.68	2.92	2.31	1.68
Basalt	6.40	1.15	2.07	1.18	0.62	2.21	1.16	0.59
Granite	6.73	1.17	1.58	1.12	0.90	1.54	1.14	0.91
Hematite	4.13	1.00	1.19	1.25	0.67	1.21	1.12	0.73
Magnetite	2.03	0.79	1.11	0.91	0.48	1.11	0.96	0.45
Mica	2.58	0.85	1.42	0.95	0.46	1.38	0.91	0.49
Milky Quartz	5.06	1.07	1.18	1.12	0.91	1.15	1.09	0.96
Quartz	5.97	1.13	1.47	1.17	0.83	1.51	1.20	0.79

**Table S.3.** Experimental and theoretical maximum forces, percentage increase in contact line due to undulations, and capillary pressures.

Particle	contact angle  (°)	maximum force (μN)			area <sup>§§</sup>  mm <sup>2</sup>	ratio <sup>*</sup>  κ	pressure  Pa
		experimental	theoretical <sup>§</sup>				
			flat	undulating			

PTFE sphere	109±5	−1305	−2150 <sup>†</sup>	—	16.31	—	−132
PTFE disc	109±5	−1292	−1961 <sup>‡</sup>	—	16.47	—	−119
PTFE tent	109±5	−1204	−1327	−1446	14.27	1.090	−93
Basalt	67±3	−537	−697	−738	9.12	1.060	−76
Granite	83±2	−467	−440	−479	4.08	1.090	−108
Hematite	95±1	−279	−396	−420	2.79	1.060	−142
Magnetite	84±2	−422	−346	−377	2.53	1.089	−137
Mica	58±3	−526	−514	−559	3.99	1.087	−129
Milky Quartz	117±2	−7	−451	−479	2.92	1.061	−155
Quartz	75±2	−402	−433	−472	4.00	1.090	−108

Theoretical calculations assuming: <sup>§</sup>ellipsoidal, <sup>†</sup>spherical or <sup>‡</sup>cylindrical shapes

<sup>§§</sup> cross-sectional area at same  $z$ -axis position where maximum force occurs

<sup>\*</sup> ratio of the length of a quadrupolarly undulating, elliptic contact line to a flat elliptic contact line

**Table S.4.** Experimental maximum and snap-off capillary forces for different particles.

Particle	contact angle ( $^{\circ}$ )	$r_{max}$ (mm)	$f_{max}$ , maximum force ( $\mu\text{N}$ )				$f_{snap-off}$ , snap-off force ( $\mu\text{N}$ )			
			Dry	Dry Clean	Wet	Wet Clean	Dry	Dry Clean	Wet	Wet Clean
PTFE sphere	$109 \pm 5$	2.79	-1305	-1022	-1163	-1048	-879	-534	-466	-329
PTFE disc	$109 \pm 5$	2.41	-1292	-1281	-1260	-1248	-1169	-778	-1207	-509
PTFE tent	$109 \pm 5$	2.99	-1204	-1081	-1023	-1037	-397	-412	-746	-562
Basalt	$67 \pm 3$	1.78	-537	-597	-525	-571	-537	-533	-312	-444
Granite	$83 \pm 2$	1.46	-467	-502	-444	-473	-427	-497	-352	-378
Hematite	$95 \pm 1$	1.23	-279	-322	-38	-251	-249	-161	-26	-200
Magnetite	$84 \pm 2$	1.16	-422	-149	-329	-49	-378	-94	-273	-49
Mica	$58 \pm 3$	1.36	-526	-43	-470	-13	-348	-39	-309	-10
Milky Quartz	$117 \pm 2$	1.01	-7	-541	-10	-529	-7	-426	-6	-272
Quartz	$75 \pm 2$	1.54	-402	-474	-377	-397	-357	-445	-268	-310

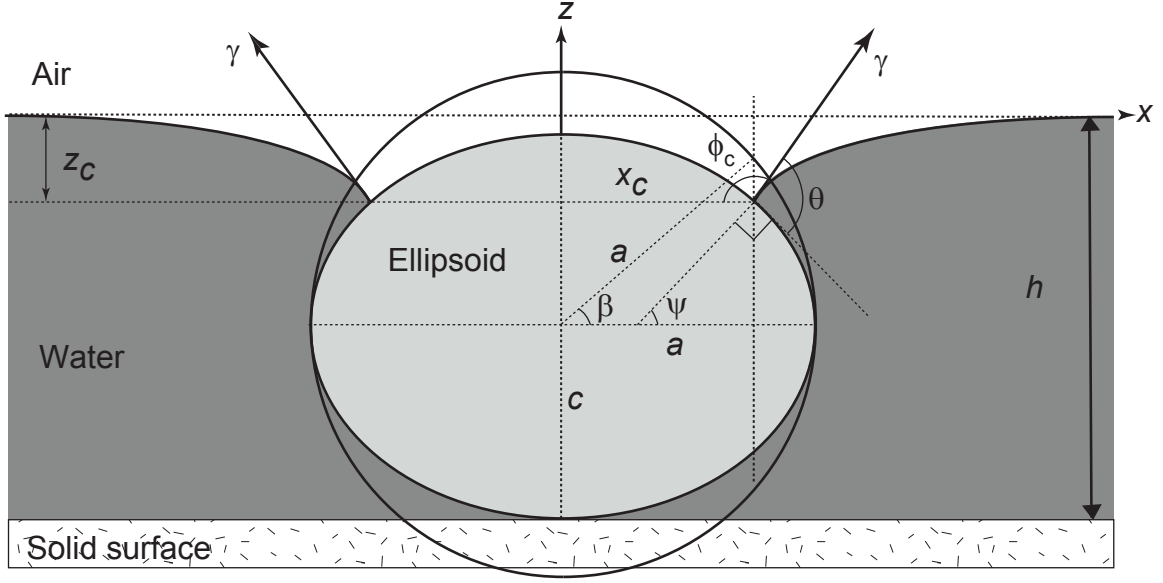


**Figure S.1.** Schematic of an ellipsoidal particle at an air-water interface.  $\theta$  is the contact angle, the angle between the tangents to the ellipsoidal particle and the air-water interface at the contact line.  $\psi$  is the geodetic latitude, the angle of the normal to the tangent at the three-phase contact line with the plane parallel to the undisturbed air-water interface containing the center of the ellipsoid.  $\beta$ ; the parametric latitude, is the angle of the projected contact line at the center of the ellipsoid. The projection is done on the surrounding sphere (of radius  $a$ , where  $a$  is the largest of the ellipsoid's semi-major axes).  $\psi = [\frac{3\pi}{2} - (\theta + \phi_c)]$ .  $\beta = \arctan[\frac{c}{a} \tan \phi]$ .

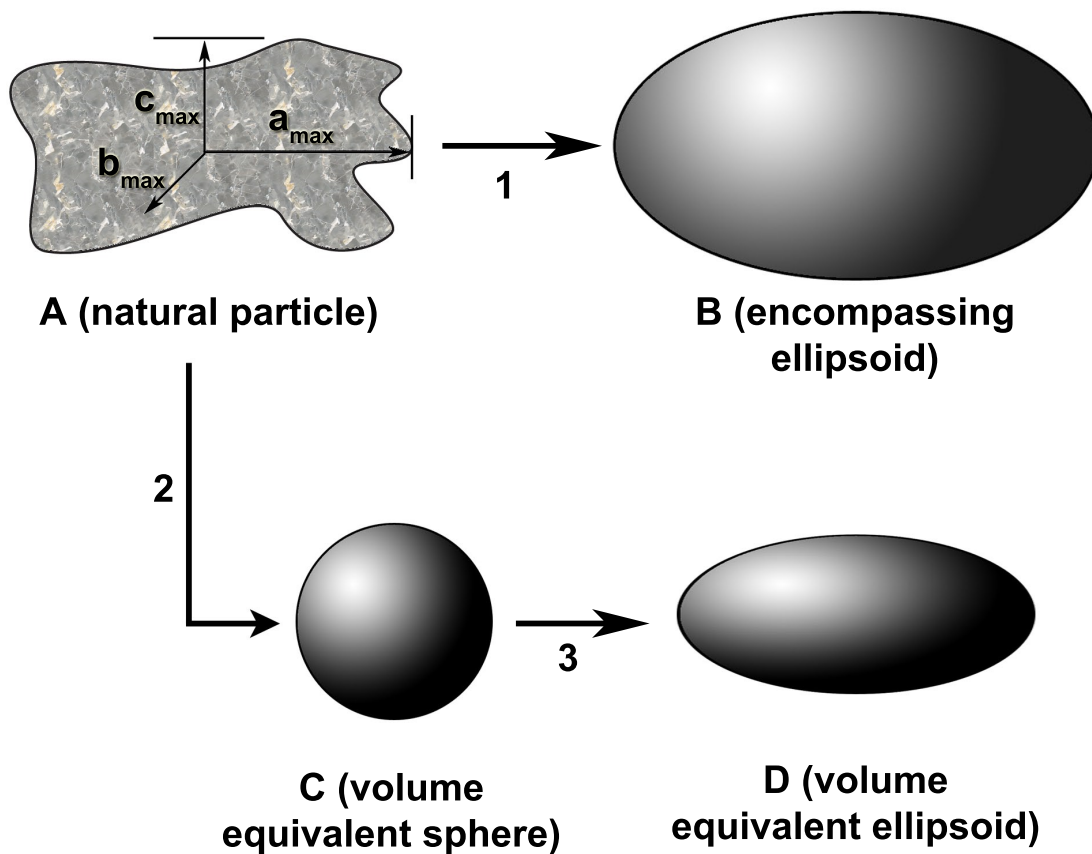


**Figure S.2.** Schematic of calculation steps to determine volume-equivalent standard shapes from the dimensions of the natural particles. (1) Define a maximum encompassing ellipsoid (B) from the  $(a, b, c)_{max}$  dimensions of the natural particle (A). The resulting particle (B) is, however, not volume equivalent with the natural particle (A). (2) Determine a volume-equivalent sphere (C) from the buoyancy force on the natural particle (A). (3) Determine a volume equivalent ellipsoid (D) using the volume of (C) and the ratios of the rms semi-major axes,  $(a, b, c)_{rms}$ .

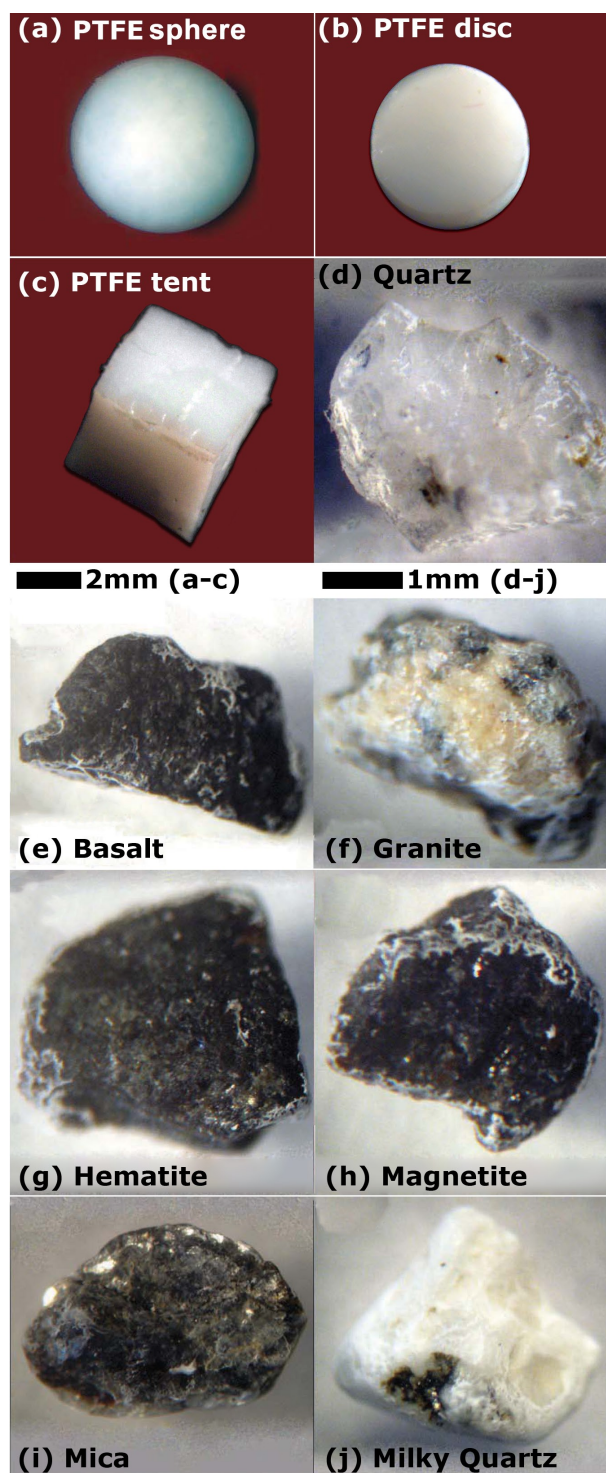


**Figure S.3.** PTFE sphere, disc and tent (a–c) and natural sediment particles (d–j) under dissection scope, viewed perpendicular to the  $xy$ -plane.

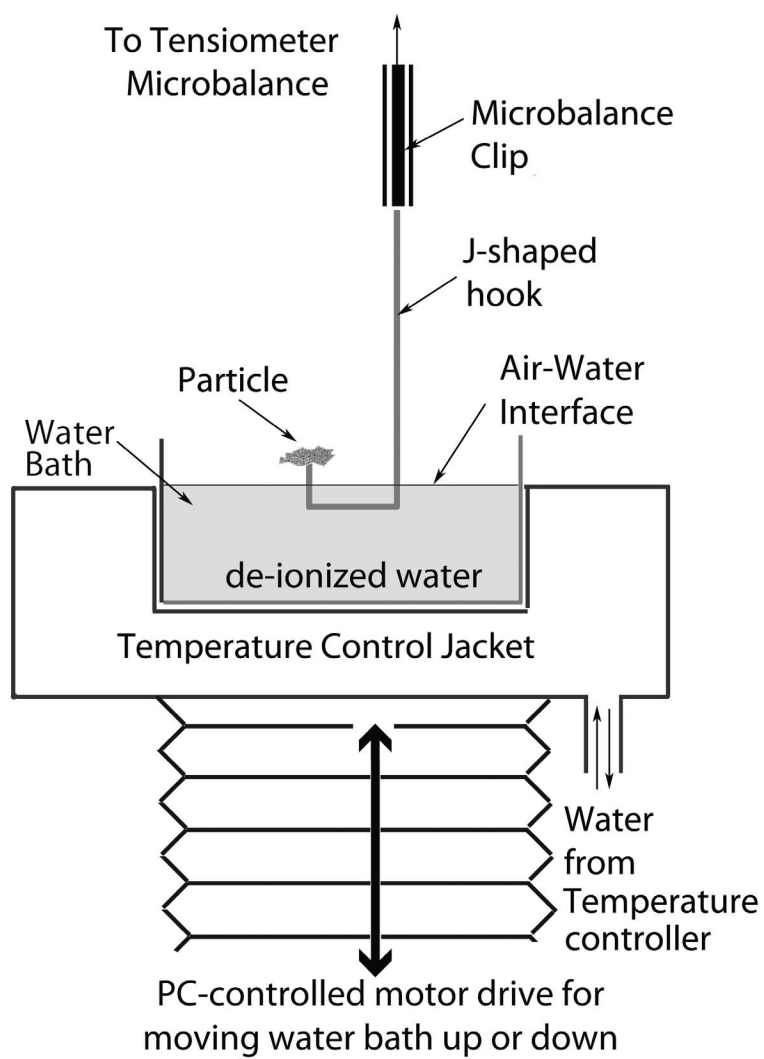


**Figure S.4.** Schematic of capillary force measurements with a process tensiometer.

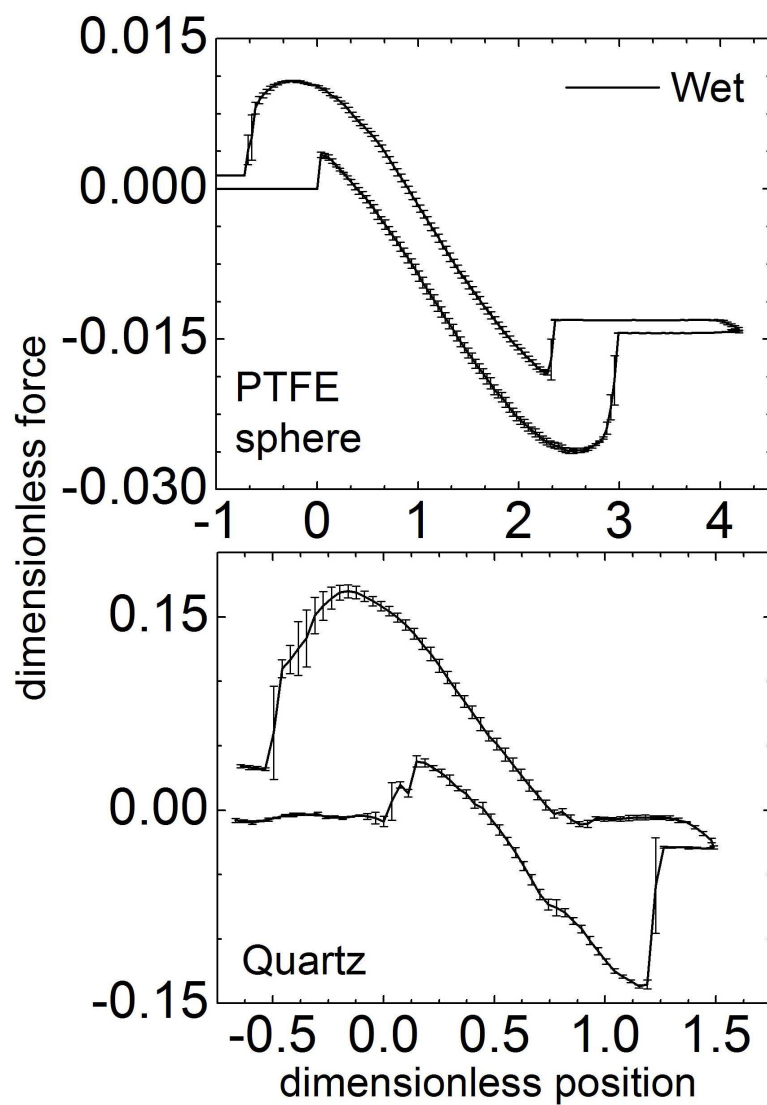


**Figure S.5.** Force-position curves illustrating measurement precision for (a) a wet PTFE sphere and (b) a wet quartz particle. Data represent the mean and  $\pm$  one standard deviation of five successive measurements.



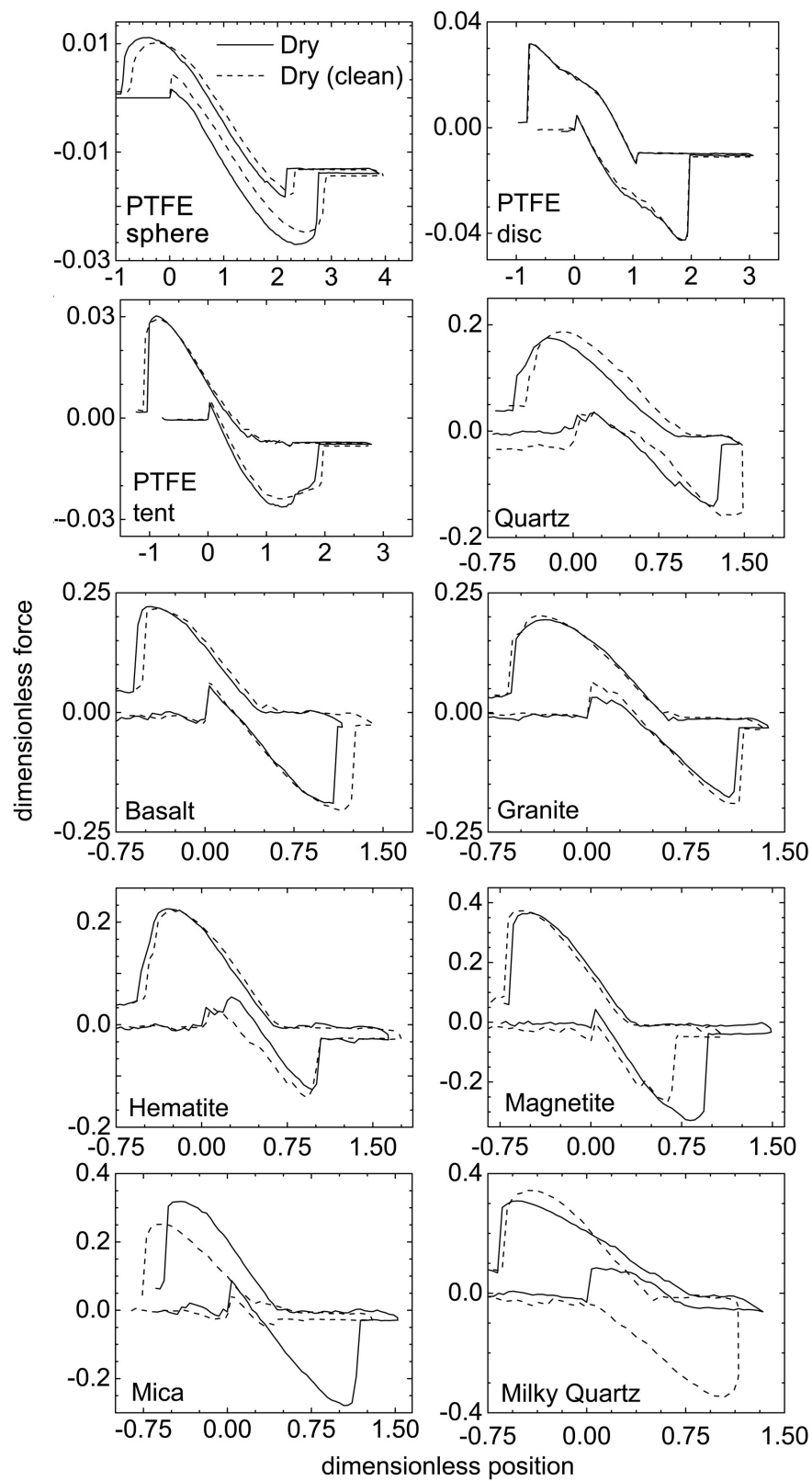


**Figure S.6.** Dimensionless force-position curves of dry PTFE particles (sphere, disc, and tent) and natural particles (both cleaned and uncleaned).

## Literature Cited

- (1) Shang, J.; Flury, M.; Deng, Y. Force measurements between particles and the air-water interface: Implications for particle mobilization in unsaturated porous media. *Water Resour. Res.* **2009**, *45*, W06420, doi:10.1029/2008WR007384.
- (2) Zhang, L.; Ren, L.; Hartland, S. More convenient and suitable methods for sphere tensiometry. *J. Colloid Interface Sci.* **1996**, *180*, 493–503.
- (3) Singh, P.; Joseph, D. D. Fluid dynamics of floating particles. *J. Fluid Mech.* **2005**, *530*, 31–80.
- (4) Brown, A. B. D.; Smith, C. G.; Rennie, A. R. Fabricating colloidal particles with photolithography and their interactions at an air-water interface. *Phys. Rev. E* Jul 2000 *62*, 951–960.
- (5) Stamou, D.; Duschl, C.; Johannsmann, D. Long-range attraction between colloidal spheres at the air-water interface: The consequence of an irregular meniscus. *Phys. Rev. E* Oct 2000 *62*, 5263–5272.
- (6) Fournier, J.-B.; Galatola, P. Anisotropic capillary interactions and jamming of colloidal particles trapped at a liquid-fluid interface. *Phys. Rev. E* Feb 2002 *65*, 031601.
- (7) Danov, K. D.; Kralchevsky, P. A.; Naydenov, B. N.; Brenn, G. Interactions between particles with an undulated contact line at a fluid interface: Capillary multipoles of arbitrary order. *Journal of Colloid and Interface Science* **2005**, *287*, 121–134.
- (8) van Nierop, E. A.; Stijnman, M. A.; Hilgenfeldt, S. Shape-induced capillary interactions of colloidal particles. *Europhys. Lett.* **2005**, *72*, 671–677.

- (9) Lehle, H.; Noruzifar, E.; Oettel, M. Ellipsoidal particles at fluid interfaces. *European Physical Journal E* **2008**, *26*, 151–160.
  
- (10) Danov, K. D.; Kralchevsky, P. A. Capillary forces between particles at a liquid interface: General theoretical approach and interactions between capillary multipoles. *Advances in Colloid and Interface Science* **2010**, *154*, 91–103.